A NOVEL APPROACH FOR AUTOMATIC FOLLOW–UP OF DETECTED LUNG NODULES

Ayman El-Baz[1]*, Georgy Gimel'farb*[2]*, Robert Falk*[3]*, and Mohamed A. El-Ghar*[4]

[1]Bioengineering Department, University of Louisville, Louisville, KY, USA.
[2]Department of Computer Science, University of Auckland, Auckland, New Zealand.
[3]Director, Medical Imaging Division, Jewish Hospital, Louisville, KY, USA.
[4]Urology and Nephrology Department, University of Mansoura, Mansoura, Egypt.

ABSTRACT

Our long term research goal is to develop an image-based approach for early diagnosis of lung nodules that may lead to lung cancer. This paper focuses on monitoring the progress of detected lung nodules in successive chest low dose CT (LDCT) scans of a patient using non-rigid registration. In this paper, we propose a new methodology for 3D LDCT data registration. The registration methodology is non-rigid and involves two steps: global alignment of one scan (target data) to another scan (reference data) using the learned prior appearance model followed by local alignments in order to correct for intricate deformations. From two subsequent chest scans, visual appearance of the chest images, after equalizing their signals, are modeled with a Markov-Gibbs random field with pairwise interaction. Our approach is based on finding the affine transformation to register one data set (target data) to another data set (reference data) by maximizing a special Gibbs energy function using a gradient descent algorithm. To get accurate appearance model, we developed a new approach to an automatically select the most important cliques that describe the visual appearance of LDCT data. To handle local deformations, we propose a new approach based on deforming each voxel over evolving closed and equi-spaced surfaces (iso-surfaces) to closely match the prototype. The evolution of the iso-surfaces is guided by an exponential speed function in the directions minimizing distances between corresponding pixel pairs on the iso-surfaces on both data sets. Our preliminary results on 10 patients show that the proper registration could lead to precise identification of the progress of the detected lung nodules.

Index Terms— Lung cancer, Low dose computed tomography, non-rigid registration, rigid registration.

1. INTRODUCTION

Because lung cancer is the most common cause of cancer deaths, fast and accurate analysis of pulmonary nodules is of major importance for medical computer-aided diagnostic systems (CAD). In [1] we introduced a fully automatic nodule detection algorithm showing the accuracy up to 93.3% on the experimental database containing 200 real LDCT chest data sets with 36,000 2D slices. In [2, 3] we introduced an accurate segmentation approach to segment the detected lung nodules from LDCT images. Below, we focus in the next CAD stage, namely, on accurate registration of the detected lung nodules for subsequent volumetric measurements to monitor how the detected lung nodules change over the time.

We use a three-step procedure to separate the nodules from their background: (*i*) an initial LDCT slice is segmented with algorithms introduced in [4] to isolate lung tissues from surrounding structures in the chest cavity as shown in Fig. 1, (*ii*) registration of two successive CT scan data sets which are taken at two different times, and

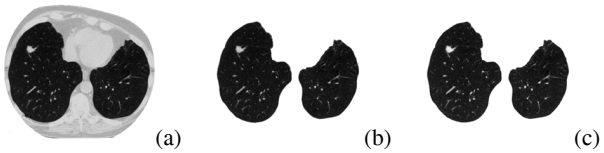

Fig. 1. Step 1 [4] of our segmentation: an LDCT slice (a) with isolated lungs (b), and (c) the normalized segmented lung image.

(*iii*) the nodules in the isolated lung regions are segmented by evolving deformable boundaries under forces that depend on the learned current and prior appearance models. At Step1 each LDCT slice is modelled as a bi-modal sample from a simple Markov–Gibbs random field of interdependent region labels and conditionally independent voxel intensities (gray levels). This step is necessary for more accurate separation of nodules from the lung tissues at Step 3 because voxels of both the nodules and other chest structures around the lungs are of quite similar intensity. In this paper we will focus on the second step.

Previous work. Tracking the temporal behavior of a nodule is a complicated task because of the change in the patient's position at each data acquisition, as well as the effects of heart beats and respiration of the patient. In order to get accurate measurements about the progress of lung nodules over the time, all this motion should be compensated by registering CT data sets taken at different time periods with each other. In the literature, many methods have been described for the medical image registration problem (see [5]), and also for the compensation of the lung motion (see [6]). Below, we will give some examples of previous work on CT lung images registration.

For the follow-up of small nodules, Brown et al. [7] developed a patient-specific model with 81% success in 27 nodules. Ko et al. [8] used the center mass point of the structures and applied rigid and affine image registration techniques with 96% success in 58 nodules of 10 patients.

To account for the non-rigid motion and deformation of the lung, Woods et al. [9] developed an objective function using an anisotropic smoothness constraint and a model based on continuum mechanics. Wood's algorithm required the detection and registration of feature points as explained in [10], and then interpolating the displacement by the model of continuum mechanics. In Wood's study, the difference of the estimated and real volumes was calculated to be 1.6%. In 2003, Dougherty et al. [11] developed an optical flow method, a model-based motion estimation technique for estimating first a global parametric transformation and then local deformations. This method allowed the alignment of serial CT images with a 95% correlation. Another optical flow analysis approach was developed

by Naqa et al. [12], where the optical flow analysis was combined with the information of a spirometer, a device measuring the airflow into and out of the lungs to track the breathing motion automatically. The spirometry approach used in Naqa's study was based on the reconstruction techniques for 4D CT during free breathing proposed by [13].

There are also studies using CT lung images for pulmonary registration. For this purpose, Zhang et al. [14] used a standard lung atlas to analyze the pulmonary structures in CT images. This atlas is registered to new images by a 3D surface based registration technique composed of global transformation and local elastic transformations. Li et al. [15] used feature points for correspondence and landmark & intensity based registration algorithms to warp a template image to the rest of the lung volumes.

2. METHODS

The objective of the proposed image analysis approach is to follow up the detected lung nodules from LDCT images. To achieve this goal, an image analysis system consisting of three steps is proposed. These steps are: 1) segmentation of lung from LDCT images, 2) a non-rigid registration approach to align two successive LDCT scans and to correct the motion artifacts caused by breathing and patient motion, and (3) segmentation of the lung nodules. *In this paper we will focus on the second step and the first and third steps are shown in details in [2–4].*

3. GLOBAL ALIGNMENT

Before describing the mathematical detail of the proposed global alignment approach, we define the following notations:
Basic notation. We denote $\mathcal{Q} = \{0, \ldots, Q-1\}$; $\mathbf{R} = [(x, y, z) : x = 0, \ldots, X-1; y = 0, \ldots, Y-1; z = 0, \ldots, Z-1]$, and $\mathbf{R}_\mathsf{p} \subset \mathbf{R}$ a finite set of scalar image signals (e.g. gray levels), a 3D arithmetic lattice supporting digital LDCT data $g : \mathbf{R} \to \mathcal{Q}$, and its arbitrary-shaped part occupied by the prototype, respectively. A finite set $\mathcal{N} = \{(\xi_1, \eta_1, \zeta_1), \ldots, (\xi_n, \eta_n, \zeta_n)\}$ of (x, y, z)-coordinate offsets defines neighbors $\{((x+\xi, y+\eta, z+\zeta), (x-\xi, y-\eta, z-\zeta)) : (\xi, \eta, \zeta) \in \mathcal{N}\} \wedge \mathbf{R}_\mathsf{p}$ interacting with each pixel $(x, y, z) \in \mathbf{R}_\mathsf{p}$. The set $\mathcal{N}$ yields a neighborhood graph on $\mathbf{R}_\mathsf{p}$ to specify translation invariant pairwise interactions with n families $\mathcal{C}_{\xi,\eta,\zeta}$ of cliques $c_{\xi,\eta,\zeta}(x, y, z) = ((x, y, z), (x+\xi, y+\eta, z+\zeta))$ (see Fig. 2). Interaction strengths are given by a vector $\mathbf{V}^\mathsf{T} = \left[\mathbf{V}^\mathsf{T}_{\xi,\eta,\zeta} : (\xi, \eta, \zeta) \in \mathcal{N}\right]$ of potentials $\mathbf{V}^\mathsf{T}_{\xi,\eta,\zeta} = \left[V_{\xi,\eta,\zeta}(q, q') : (q, q') \in \mathcal{Q}^2\right]$ depending on signal co-occurrences; here T indicates transposition.

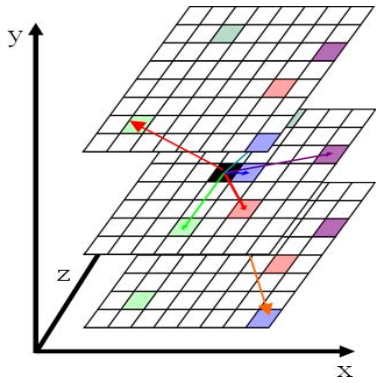

Fig. 2. Pairwise pixel interaction MGRF model.

3.1. Data Normalization

To account for monotone (order-preserving) changes of signals (e.g. due to different illumination or sensor characteristics), the LDCT images are equalized using the cumulative empirical probability distributions of their signals.

3.2. MGRF based appearance model

Generic MGRF with multiple pairwise interaction (Fig. 2) [4, 16], the Gibbs probability $P(g) \propto \exp(E(g))$ of an object g aligned with the prototype g° on $\mathbf{R}_\mathsf{p}$ is specified with the Gibbs energy

$$E(g) = |\mathbf{R}_\mathsf{p}| \mathbf{V}^\mathsf{T} \mathbf{F}(g) \tag{1}$$

where $\mathbf{F}^\mathsf{T}(g)$ is the vector of scaled empirical probability distributions of signal co-occurrences over each clique family: $\mathbf{F}^\mathsf{T}(g) = [\rho_{\xi,\eta,\zeta} \mathbf{F}^\mathsf{T}_{\xi,\eta,\zeta}(g) : (\xi, \eta, \zeta) \in \mathcal{N}]$ where $\rho_{\xi,\eta,\zeta} = \frac{|\mathcal{C}_{\xi,\eta,\zeta}|}{|\mathbf{R}_\mathsf{p}|}$ is the relative size of the family and $\mathbf{F}_{\xi,\eta,\zeta}(g) = [f_{\xi,\eta,\zeta}(q, q'|g) : (q, q') \in \mathcal{Q}^2]^\mathsf{T}$; here, $f_{\xi,\eta,\zeta}(q, q'|g) = \frac{|\mathcal{C}_{\xi,\eta,\zeta;q,q'}(g)|}{|\mathcal{C}_{\xi,\eta,\zeta}|}$ are empirical probabilities of signal co-occurrences, and $\mathcal{C}_{\xi,\eta,\zeta;q,q'}(g) \subseteq \mathcal{C}_{\xi,\eta,\zeta}$ is a subfamily of the cliques $c_{\xi,\eta,\zeta}(x, y, z)$ supporting the co-occurrence $(g_{x,y,z} = q, g_{x+\xi,y+\eta,z+\zeta} = q')$ in g. The co-occurrence distributions and the Gibbs energy for the object are determined over $\mathbf{R}_\mathsf{p}$, i.e. within the prototype boundary after an object is affinely aligned with the prototype. To account for the affine transformation, the initial image is resampled to the back-projected $\mathbf{R}_\mathsf{p}$ by interpolation.

The appearance model consists of the neighborhood $\mathcal{N}$ and the potential $\mathbf{V}$ to be learned from the prototype.

Learning the potentials: The MLE of $\mathbf{V}$ is proportional in the first approximation to the scaled centered empirical co-occurrence distributions for the prototype [16]:

$$\mathbf{V}_{\xi,\eta,\zeta} = \lambda \rho_{\xi,\eta,\zeta} \left(\mathbf{F}_{\xi,\eta,\zeta}(g^\circ) - \frac{1}{Q^2} \mathbf{U} \right); \ (\xi, \eta, \zeta) \in \mathcal{N}$$

where $\mathbf{U}$ is the vector with unit components. The common scaling factor λ is also computed analytically; it is approximately equal to Q^2 if $Q \gg 1$ and $\rho_{\xi,\eta,\zeta} \approx 1$ for all $(\xi, \eta, \zeta) \in \mathcal{N}$. In our case it can be set to $\lambda = 1$ because the registration uses only relative potential values and energies.

Learning the characteristic neighbors: To find the characteristic neighborhood set $\mathcal{N}$, the relative energies $E_{\xi,\eta,\zeta}(g^\circ) = \rho_{\xi,\eta,\zeta} \mathbf{V}^\mathsf{T}_{\xi,\eta,\zeta} \mathbf{F}_{\xi,\eta,\zeta}(g^\circ)$ for the clique families, i.e. the scaled variances of the corresponding empirical co-occurrence distributions, are compared for a large number of possible candidates. To automatically select the characteristic neighbors, we consider an empirical probability distribution of the energies as a mixture of a large "non-characteristic" low-energy component and a considerably smaller characteristic high-energy component: $P(E) = \pi P_\mathrm{lo}(E) + (1-\pi) P_\mathrm{hi}(E)$. Both the components $P_\mathrm{lo}(E)$, $P_\mathrm{hi}(E)$ are of arbitrary shape and thus are approximated with linear combinations of positive and negative discrete Gaussians (efficient EM-based algorithms introduced in [4, 16] are used for both the approximation and estimation of π).

Appearance-based registration: The object g is affinely transformed to (locally) maximize its relative energy $E(g_\mathbf{a}) = \mathbf{V}^\mathsf{T} \mathbf{F}(g_\mathbf{a})$ under the learned appearance model $[\mathcal{N}, \mathbf{V}]$. Here, $g_\mathbf{a}$ is the part of the object image reduced to $\mathbf{R}_\mathsf{p}$ by the affine transformation $\mathbf{a} = [a_{11}, \ldots, a_{23}]$: $x' = a_{11}x + a_{12}y + a_{13}z + a_{14}$; $y' = a_{21}x + a_{22}y + a_{23}z + a_{24}$; $z' = a_{31}x + a_{32}y + a_{33}z + a_{34}$. The initial transformation is a pure translation with $a_{11} = a_{22} = 1$;

$a_{12} = a_{21} = 0$, ensuring the most "energetic" overlap between the object and prototype. Then the gradient search for the local energy maximum closest to the initialization selects the 12 parameters $\mathbf{a}$.

4. LOCAL MOTION MODEL

To handle local deformations, we propose a new approach based on deforming the object over evolving closed and equi-spaced contours/surfaces (iso-contours/surfaces) to closely match the prototype. The evolution of the iso-contours/surfaces is guided by an exponential speed function in the directions minimizing distances between corresponding pixel pairs on the iso-contours/surfaces on both images. The normalized cross correlation is used to find the correspondent points between these iso-contours/surfaces.

The first step of our approach is to generate the distance map inside the object using fast marching level sets [17]. The second step is to use this distance map to generate iso-surfaces (Fig. 3). Note that the number of iso-contours/surfaces, which is not necessarily the same for both images, depends on the accuracy and the speed required by the user. The third step consists in finding the correspondences between the iso-surfaces using normalized cross correlation. The final step is the evolution of the iso-surfaces; here, our goal is to deform the iso-surfaces in the first data set (target image) to match the iso-surfaces in the second data set (reference image). Before stating the evolution equation, let us define the following:

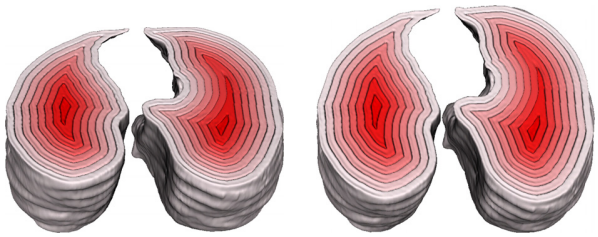

(a) Reference data (b) Target data

Fig. 3. Equal spaced generated surfaces.

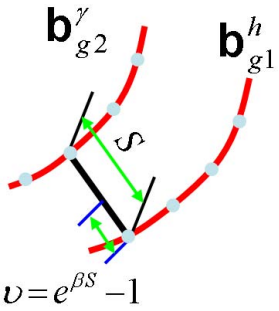

Fig. 4. Evolution scenario.

- $\mathbf{b}^{h}_{\mathbf{g}_1} = [\mathbf{p}^{h}_{k} : k = 1, \ldots, K]$ – K control points on surface h on the reference data, $\mathbf{p}_k = (x_k, y_k, z_k)$ forming a circularly connected chain of line segments $(\mathbf{p}_1, \mathbf{p}_2)$, …, $(\mathbf{p}_{K-1}, \mathbf{p}_K)$, $(\mathbf{p}_K, \mathbf{p}_1)$.
- $\mathbf{b}^{\gamma}_{\mathbf{g}_2} = [\mathbf{p}^{\gamma}_{n} : n = 1, \ldots, N]$ – N control points on surface γ on the target data, $\mathbf{p}_n = (x_n, y_n, z_n)$ forming a circularly connected chain of line segments $(\mathbf{p}_1, \mathbf{p}_2)$, …, $(\mathbf{p}_{N-1}, \mathbf{p}_N)$, $(\mathbf{p}_N, \mathbf{p}_1)$.
- $S(\mathbf{P}^{h}_{k}, \mathbf{P}^{\gamma}_{n})$ denotes the Euclidean distance between a point on surface h in image $\mathbf{g}_1$ and its corresponding point on surface γ in image $\mathbf{g}_2$,
- $S(\mathbf{P}^{\gamma}_{n}, \mathbf{P}^{\gamma-1}_{n})$ denotes the Euclidean distance between a point on surface γ in image $\mathbf{g}_1$ and its nearset point on surface $\gamma - 1$ in image $\mathbf{g}_1$
- $\nu(.)$ is the propagation speed function .

The evolution $\mathbf{b}_\tau \rightarrow \mathbf{b}_{\tau+1}$ of the deformable boundary $\mathbf{b}$ in discrete time, $\tau = 0, 1, \ldots$, is specified by the system of difference equations $\mathbf{p}^{\gamma}_{n,\tau+1} = \mathbf{p}^{\gamma}_{n,\tau} + \nu(P^{\gamma}_{n,\tau})\mathbf{u}_{n,\tau};\ n = 1, \ldots, N$, where $\nu(P^{\gamma}_{n,\tau})$ is a propagation speed function for the control point $\mathbf{P}^{\gamma}_{\mathbf{n},\tau}$ and $\mathbf{u}_{n,\tau}$ is the unit vector along the ray between two correspondant points. The propagation speed function is selected so as to satisfy the following conditions: $\nu(P^{\gamma}_{n,\tau}) = 0$ if $S(\mathbf{P}^{h}_{k}, \mathbf{P}^{\gamma}_{n,\tau})$ = 0, otherwise $\nu(P^{\gamma}_{n,\tau}) = \min\left[S(\mathbf{P}^{h}_{k}, \mathbf{P}^{\gamma}_{n,\tau}), S(\mathbf{P}^{\gamma}_{n,\tau}, \mathbf{P}^{\gamma-1}_{n,\tau}), S(\mathbf{P}^{\gamma}_{n,\tau}, \mathbf{P}^{\gamma+1}_{n,\tau})\right]$. The latter condition, known as the smoothness constraint, prevents the current point from cross-passing the closest neighbor surfaces as shown in Fig. 4. Note that the function $\nu(P^{\gamma}_{n,\tau}) = -1 + exp\big(\beta(\mathbf{P}^{\gamma}_{n,\tau})S(\mathbf{P}^{h}_{k}, \mathbf{P}^{\gamma}_{n,\tau})\big)$; satisfies the above conditions, where $\beta(\mathbf{P}^{\gamma}_{n,\tau})$ is the propagation term such as, at each surface point $\beta(\mathbf{P}^{\gamma}_{n,\tau}) = \frac{\ln\left(\min\left[S(\mathbf{P}^{h}_{k}, \mathbf{P}^{\gamma}_{n,\tau}), S(\mathbf{P}^{\gamma}_{n,\tau}, \mathbf{P}^{\gamma-1}_{n,\tau}), S(\mathbf{P}^{\gamma}_{n,\tau}, \mathbf{P}^{\gamma+1}_{n,\tau})\right]+1\right)}{S(\mathbf{P}^{h}_{k}, \mathbf{P}^{\gamma}_{n,\tau})}$.

5. EXPERIMENTAL RESULTS AND CONCLUSIONS

The proposed non-registration approach is tested on clinical datasets collected from 10 patients. Each patient has five scans, and the period between each two successive CT scans is three months. This preliminary clinical database collected by low dose CT scan protocol with the following scanning parameters: slice thickness of 2.5 mm reconstructed every 1.5 mm, scanning pitch 1.5, pitch 1 mm, KV 140, MA 100, and F.O.V 36 cm. Figure 5(d) shows checkerboard visualization between the data sets shown in Fig. 5(a) and the aligned data set shown in Fig. 5(c) to demonstrate the effect of the motion of the lung tissues. It can be seen that the connectivity at the edges of the lung, between the two volumes is not smooth when using the global model only, this is due to the local deformation which comes from breathing and heart beats. Figure 5 shows the results after applying the local deformation model. It shows the connectivity at the edges of lung region, and between the two volumes is smoother when using the proposed local deformation model.

After the two volumes of different time instants are registered, the task is to find out if the nodules are growing or not. For this purpose, after registration, we are segmenting the lung nodules using our previous approach [2, 3]. Once the nodules are segmented in the original and registered image sequences, the volumes of the nodules are calculated using the Δx, Δy, and Δz values from the scanner. In our studies, these values are $0.7mm$, $0.7mm$, and $2.5mm$ respectively. Figure 6 shows the detected changes in two detected lung nodules for two different patients over one year.

In this paper, we introduced a new approach for the non-rigid registration of spiral LDCT images. The proposed algorithm consist of two steps: global alignment of one scan (target data) to another scan (reference data) using the learned prior appearance model followed by local alignments in order to correct for intricate deformations. The preliminary results on 10 patients show that the proper registration could lead to precise identification of the progress of the detected lung nodules.

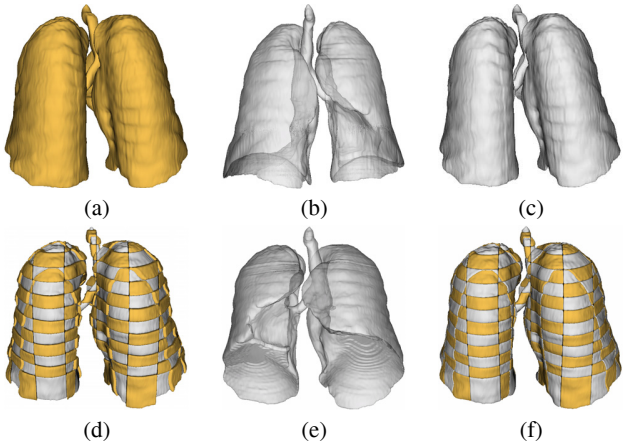

Fig. 5. (a) Reference data, (b) target data, (c) transformed data using 12 degree of freedom affine transformation, (d) checkerboard visualization to show the motion effect of the lung tissues, (e) our non-rigid regeneration results, and (g) checkerboard visualization to show the quality of the proposed local deformation model.

Patient #1				
Scanning periods	After 3 months	After 6 months	After 9 months	After 12 months
Before Alignment				
ΔV	7.91%	28.7%	49.2 %	121.9%
After Alignment				
ΔV	27.3%	68.9%	113.5 %	151.9%
Patient #2				
Scanning periods	After 3 months	After 6 months	After 9 months	After 12 months
Before Alignment				
ΔV	0.96%	1.7%	5.71%	8.9%
After Alignment		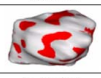	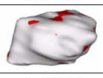	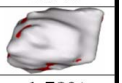
ΔV	0.14%	0.81%	1.12%	1.79%

Fig. 6. The results of the proposed follow up registration algorithm for two patients over one year

6. REFERENCES

[1] A. A. Farag, A. El-Baz, and G. Gimelfarb, "Quantitative Nodule Detection in Low Dose Chest CT Scans: New Template Modeling and Evaluation for CAD System Design," *Proc. of International Conference on Medical Image Computing and Computer-Assisted Intervention (MICCAI)*, Palm Springs, California, USA, October 26-29, 2005, pp. 720-728.

[2] A. Farag, A. El-Baz, G. Gimel'farb, R. Falk, M. Abou El-Ghar, T. Eldiasty, S. Elshazly, "Appearance Models for Robust Segmentation of Pulmonary Nodules in 3D LDCT Chest Images," *Proc. of International Conference on Medical Image Computing and Computer–Assisted Intervention (MICCAI'06),* Copenhagen, Denmark, October 1–6, 2006, pp. 662-670.

[3] A. El-Baz, A. A. Farag, G. L. Gimel'farb, R. Falk, M. Abou El-Ghar, T. Eldiasty, A Framework for Automatic Segmentation of Lung Nodules from Low Dose Chest CT Scans, Proc. of IEEE International Conference on Pattern Recognition (ICPR06), Hong Kong, August 2024, 2006, pp. 611-614.

[4] A. A. Farag, A. El-Baz, and G. Gimel'farb, "Precise Segmentation of Multi-modal Images," *IEEE Transactions on Image Processing*, vol. 15, no. 4, pp. 952-968, April 2006.

[5] J. B. A. Maintz and M. A. Viergever, "A Survey of Medical Image Registration," *Medical Image Analysis*, vol.2, pp.1–36, 1998.

[6] J. Ko and D. Naidich, "Computer-aided diagnosis and the evaluation of lung disease," *Journal of thoracic imaging*, pp. 19–136, 2004.

[7] M. Brown, M. McNitt-Gray, N. Mankovich et al., "Method for segmenting chest CT image data using an anatomical model: preliminary results," *IEEE Trans Med Imaging*, vol. 20, pp. 242-1250, 2001.

[8] J. Ko, and M. Betke, "Chest CT: automated nodule detection and assessment of change over timepreliminary experience," *Radiology*, vol. 218, pp. 267–273, 2001.

[9] K. Woods, L. Fan, C. W. Chen, and Y. Wang, "Model Supported Image Registration and Warping for Change Detection in Computer-aided Diagnosis," *Applied Imagery Pattern Recognition (AIPR) Annual Workshops*, Washington DC, 2000.

[10] L. Fan and C. W. Chen, "An integrated approach to 3D warping and registration from lung images," *Proceedings of SPIE Conf. Developments in X-Ray Tomography II*, Denver, CO, July 1999.

[11] L. Dougherty, J. Asmuth and W. Gefter, "Alignment of CT lung volumes with an optical flow method," *Academic radiology*, vol. 10, pp. 249–254, 2003.

[12] I. Naqa, D. Low, J. Deasy et al., "Automated breathing motion tracking for 4D computed tomography," *Nuclear Science Symposium Conference Record*, vol. 5,pp. 3219–3222, 2003.

[13] D. Low et al., "A method for the reconstruction of four-dimensional synchronized CT scans acquired during free breathing," *Medical Physics*, vol. 30, No. 6, 2003.

[14] L. Zhang and J. Reinhardt, "3D pulmonary CT image registration with a standard lung atlas," *Proc. SPIE Conf. Medical Imaging*, 4322, pp. 67-77, 2000.

[15] B. Li, G. E. Christensen, J. Dill, E. A. Hoffman, and J. M. Reinhardt, "3-D inter-subject warping and registration of pulmonary CT images for a human lung model," *Proc. SPIE Conf. Medical Imaging*, vol. 4683, pp. 324–335, San Diego, CA, 2002.

[16] A. El-Baz, A. Ali, A. A. Farag, G. L. Gimel'farb, "A Novel Approach for Image Alignment Using a Markov-Gibbs Appearance Model," *Proc. of International Conference on Medical Image Computing and Computer-Assisted Intervention (MICCAI'06)*, Copenhagen, Denmark, October 1–6, 2006, pp. 734–741.

[17] J. A. Sethian, "Fast marching level set method for monotonically advancing fronts," *Proc. Nat. Acad. Sci., USA*, vol. 93, pp. 1591–1595, Feb. 1996.